Nano Research 2016, 9(7): 2034–2045
DOI 10.1007/s12274-016-1094-x
Research Article
ISSN 1998-0124
CN 11-5974/O4

Self-healing superhydrophobic polyvinylidene fluoride/Fe_3O_4@polypyrrole fiber with core–sheath structures for superior microwave absorption

Yunan Li[1], Yong Zhao[1], Xianyong Lu[1] (✉), Ying Zhu[1] (✉), and Lei Jiang[1,2]

[1] *Key Laboratory of Bio-inspired Smart Interfacial Science and Technology of Ministry of Education, School of Chemistry and Environment, Beihang University, Beijing 100191,China*
[2] *Laboratory of Bio-inspired Smart Interfacial Science, Technology Institute of Physics and Chemistry, Chinese Academy of Science, Beijing 100190, China*

Received: 1 February 2016
Revised: 22 March 2016
Accepted: 6 April 2016

KEYWORDS
self-healing, superhydrophobicity, core–sheath structure, microwave absorption

ABSTRACT

Self-healing superhydrophobic polyvinylidene fluoride/Fe_3O_4@polypyrrole (F-PVDF/Fe_3O_4@PPy_x) fibers with core–sheath structure were successfully fabricated by electrospinning of a PVDF/Fe_3O_4 mixture and *in situ* chemical oxidative polymerization of pyrrole, followed by chemical vapor deposition with fluoroalkyl silane. The F-PVDF/Fe_3O_4@$PPy_{0.075}$ fiber film produces a superhydrophobic surface with self-healing behavior, which can repetitively and automatically restore superhydrophobicity when the surface is chemically damaged. Moreover, the maximum reflection loss (R_L) of the F-PVDF/Fe_3O_4@$PPy_{0.075}$ fiber film reaches –21.5 dB at 16.8 GHz and the R_L below –10 dB is in the frequency range of 10.6–16.5 GHz with a thickness of 2.5 mm. The microwave absorption performance is attributed to the synergetic effect between dielectric loss and magnetic loss originating from PPy, PVDF and Fe_3O_4. As a consequence, preparing such F-PVDF/Fe_3O_4@PPy_x fibers in this manner provides a simple and effective route to develop multi-functional microwave absorbing materials for practical applications.

1 Introduction

With the increasing use of electronic and communication devices, electromagnetic interference (EMI) has become a serious issue in both civil and military applications, which can not only impact human health, but also impede normal function of electronic devices [1, 2]. To overcome EMI issues, high-performance microwave absorbing materials (MAMs) are needed, that can effectively absorb electromagnetic (EM) waves and convert EM energy into thermal energy or dissipate the EM waves by interference [3, 4]. According to dissipation mechanisms, MAMs can be categorized into dielectric loss and magnetic loss MAMs [5]. Among MAMs, conducting polymers, including polyaniline (PANI), polypyrrole (PPy) and

Address correspondence to Xianyong Lu, xylu@buaa.edu.cn; Ying Zhu, zhuying@buaa.edu.cn

poly(3,4-ethylenedioxythiophene) (PEDOT) as dielectric loss materials represent the most attractive candidates due to their unique properties, such as ease of preparation, relatively low density, facile processing and adjustable electrical properties by doping nature and degree [6–9]. For example, Oyharcabal et al. prepared conductive epoxy composites containing PANI with globular, fibrillar or flake-like morphologies. The maximum reflection loss (R_L) of composites containing flake-like PANI was –37 dB, whereas the R_L values with fibrillar PANI and globular PANI were –8 and –7 dB, respectively [7]. Based on classical EM theory, EM absorption properties are strongly dependent on dielectric loss and magnetic loss, as well as their impedance matching characteristics [10]. Unfortunately, conducting polymers show enhanced dielectric loss but low magnetic loss, which may result in poor impedance matching, weak microwave absorption or narrow absorption bandwidth [11–13], further limiting their practical applications. Therefore, constructing conducting polymer-based nanocomposites by combining dielectric loss with magnetic loss could be an effective way to improve impedance matching, broaden absorption bandwidth, and enhance absorption intensity. Thanks to their high stability and other inherent properties, ferrite nanoparticles have been effectively employed as fillers to enhance the microwave absorption efficiency of composites. For instance, Fe_3O_4-PANI nanoparticles with core–shell structures were prepared by an *in situ* polymerization, which provided an optimal R_L of –35.1 dB at 16.7 GHz with a 1.7 mm thick layer [8]. Zhou et al. synthesized highly regulated core–shell Fe_3O_4-PEDOT microspheres by a two-step approach, which exhibited excellent microwave absorbing behavior with a minimum R_L of –30 dB at 9.5 GHz [9]. Although considerable progress has been made in conducting polymer composites, a simple scalable method for fabricating efficient MAMs with well-defined structures would be beneficial for their practical applications.

In practical applications, however, MAMs work in harsh environments including high humidity, harsh acidic or alkaline conditions, which may cause performance degradation in EM absorption due to physical or chemical damage. Therefore, it is required that MAMs have special wettability for these harsh environments. Superhydrophobic surfaces with water contact angle (CA) > 150° display extreme water repellent properties, and can cause water to bead up and roll straight off the surface with any dirt and grime [14, 15], useful behavior in a wide range of applications from self-cleaning surfaces to corrosion-resistant and anti-adhesive coatings [16]. However, the poor durability of artificial superhydrophobic surfaces severely hinders their practical applications. Inspired by the ability of lotus leaves to regenerate their superhydrophobicity against physical damage, the combination of superhydrophobic and self-healing properties may prove an effective means to solve this problem [16]. For example, Zhou et al. prepared a robust, superamphiphobic fabric with self-healing ability by a two-step wet-chemistry coating technique. After being damaged by plasma treatment, the fabric could restore its super liquid-repellent properties by a brief heating treatment or room temperature aging [17]. Li et al. fabricated superhydrophobic coatings by chemical vapor deposition (CVD) of a fluoroalkyl saline (FAS) on the surface of an assembled porous polymer, which displayed repeatable self-healing without decreases in the superhydrophobicity [16]. However, while MAMs with self-healing and water-repellent properties have been infrequently reported, they are important for broadening their future applications.

Herein, we have successfully fabricated a self-healing superhydrophobic polyvinylidene fluoride (PVDF)/Fe_3O_4@PPy fiber with core–sheath structure by electrospinning of a PVDF/Fe_3O_4 mixture and *in situ* chemical oxidative polymerization of pyrrole monomers, followed by CVD of FAS, denoted as a F-PVDF/Fe_3O_4@PPy_x film (x represents the feeding weight of pyrrole). The F-PVDF/Fe_3O_4@$PPy_{0.075}$ film typically has a water CA of 152.0° ± 0.5° and sliding angle of 6.5°, showing self-cleaning superhydrophobicity. In particular, after air plasma etching treatment of F-PVDF/Fe_3O_4@$PPy_{0.075}$, the film automatically restores its superhydrophobicity when left under a medium relative humidity (RH), exhibiting self-healing superhydrophobic ability. As expected, the F-PVDF/Fe_3O_4@$PPy_{0.075}$ film also displays superior microwave absorption, with a maximum R_L value of –21.5 dB at 16.8 GHz, where a R_L below –10 dB is present between 10.6 and 16.5 GHz at 2.5 mm thickness.

We believe that self-healing superhydrophobic F-PVDF/Fe_3O_4@PPy_x fiber with core–sheath structure is a promising candidate for effective microwave absorbers working under harsh environments.

2 Experimental

2.1 Materials

Pyrrole,1H,1H,2H,2H-perfluorodecyltriethoxysilane (FAS) and PVDF powder (M_W = 530,000) were obtained from J&K Chemical Company. Pyrrole was distilled under reduced pressure before use. Iron acetylacetonate ($Fe(acac)_3$) was purchased from Aldrich and used after a 2-fold recrystallization. Triethylene glycol (TEG), polyvinylpyrrolidone (PVP, M_W = 40,000), N,N-dimethylacetamide (DMAc), sodium dodecylbenzene sulfonate (SDBS), ferric chloride ($FeCl_3$), ether, ethanol and acetone were commercially available products. All other chemicals of analytical grade were used as received.

2.2 Preparation of Fe_3O_4 nanoparticles

Fe_3O_4 nanoparticles were synthesized according to a previously published method [18, 19]. In a typical synthesis, 12 mmol $Fe(acac)_3$ (organic metal precursor) and 0.12 mmol PVP (stabilizer) were mixed with 120 mL of TEG (high boiling point solvent) by strong mechanical stirring at room temperature. The mixture was heated to 60 ℃ under N_2 and held for 1 h to eliminate oxygen completely, and then heated to 270 ℃ for 2 h to form a black dispersion. After cooling down to room temperature, this black dispersion was precipitated using ether (500 mL) and separated by a permanent magnet. This black precipitate was re-dispersed through ultrasonic treatment in ethanol (20 mL) and re-precipitated by adding 100 mL ether. After repeating the aforementioned procedures three times, Fe_3O_4 nanoparticles were eventually obtained and dispersed in ethanol for further use. Characterization of the Fe_3O_4 nanoparticles is shown in Fig. S1 in the Electronic Supplementary Material (ESM).

2.3 Fabrication of PVDF/Fe_3O_4 fiber film

PVDF/Fe_3O_4 fiber film was fabricated by electrospinning. First, a 4.5 wt.% Fe_3O_4 dispersion was prepared by adding 0.16 g Fe_3O_4 nanoparticles to a mixture of DMAc and acetone (7:3 w/w) under ultrasonic treatment for 0.5 h, then 0.48 g PVDF powder was dissolved into the dispersion under stirring for at least 4 h to form a homogenous mixed solution. Second, the mixed solution was loaded into a 5 mL plastic syringe equipped with a stainless-steel needle, which was connected to a high voltage power supply (FL 32174, Gamma). A working voltage of 22 kV was applied and a piece of aluminum foil was placed about 25 cm below the tip of the needle to collect the PVDF/Fe_3O_4 fiber film. Finally, the film was then placed in a vacuum oven at 60 ℃ for 12 h.

2.4 Fabrication of self-healing superhydrophobic F-PVDF/Fe_3O_4@PPy fiber with core–sheath structure

PVDF/Fe_3O_4@PPy_x fibers with core–sheath structures (where x represents the feeding weight of pyrrole) were prepared through *in situ* chemical oxidative polymerization of pyrrole monomers in the presence of an electrospun PVDF/Fe_3O_4 fiber film as a substrate, with $FeCl_3$ as an oxidant at room temperature. Typically, 0.01 g SDBS and 0.075 g pyrrole were added to 50 mL of deionized water and ultrasonicated for 10 min, then 0.1 g PVDF/Fe_3O_4 membrane was immersed in the mixture under stirring. After the mixture was stirred for 2 h, 5 mL $FeCl_3$ aqueous solution (molar ratio of $FeCl_3$:pyrrole is 1:1) was directly added to initiate polymerization, and the reaction solution was stirred for another 2 h. Finally, the resultant PVDF/Fe_3O_4@$PPy_{0.075}$ film was thoroughly rinsed with deionized water three times and dried in an oven at 80 ℃ for 6 h. The PVDF/Fe_3O_4@$PPy_{0.05}$ and PVDF/Fe_3O_4@$PPy_{0.10}$ films were fabricated using the same procedure as the PVDF/Fe_3O_4@$PPy_{0.075}$ film, except that 0.05 and 0.10 g of pyrrole monomer were supplied, respectively. To obtain the self-healing and superhydrophobic properties, the PVDF/Fe_3O_4@PPy_x films were placed in a desiccator containing several drops of FAS under continuous vacuum for 12 h, and the obtained films were denoted as F-PVDF/Fe_3O_4@PPy_x films.

2.5 Characterization

Powder X-ray diffraction (XRD) patterns were obtained with a Shimadzu X-ray Diffractometer (XRD-6000)

equipped with a Cu-Ka1 source (λ = 1.5406 Å). Scanning electron microscopy (SEM) studies were done with a field emission JSM-7500F operating at an accelerating voltage of 20 kV. Transmission electron microscopy (TEM), and energy-dispersive X-ray spectroscopy (EDS) mapping were performed with a JEM-2100F working at an accelerating voltage of 200 kV. Fourier transform infrared spectroscopy (FT-IR) was recorded on an infrared microspectrometer (iN10MX, Nicolet) in the range of 4,000–500 cm^{-1}. The electrical conductivity was measured using a standard four-probe method on a KDY-1 resistivity/sheet resistance tester (Kunde, China). Thermogravimetric analysis (TGA) of the samples was performed on a thermogravimetric analyzer (NETZSCH, STA 449 F3) from 30 to 800 °C at a heating rate of 10 °C·min^{-1} under air. Contact angles were measured on a contact angle system (OCA20, Dataphysics, Germany) by dropping water (4 μL) onto the samples at ambient temperature. Average contact angles were obtained by measuring the same sample at five different positions. Sliding angles were measured by dropping water (10 μL) onto the sample at ambient temperature. Air plasma etchings were conducted using a PDC-32G plasma cleaner (Harrick Plasma) under 70 Pa at room temperature. Corrosion resistance experiments were carried out in a three electrode configuration using a platinum plate and Ag/AgCl electrode as the counter and reference electrode, respectively. The as-prepared film was used as a working electrode. Measurements were performed in a 3.5 wt.% NaCl aqueous solution using a CHI 760E electrochemical workstation (CHI Instruments, China) at room temperature. Electrochemical impedance spectroscopy (EIS) measurements were conducted in the frequency range between 10 mHz and 100 kHz with a potential amplitude of 5 mV. Magnetic properties were examined with a vibrating sample magnetometer (VSM, LakeShore 7307) at room temperature. The samples used for EM absorption measurements were repeatedly folded and further hot-pressured into toroidal-shaped specimens with thickness of 2 mm (outer diameter: 7.00 mm, inner diameter: 3.04 mm) by a manual sheeter at 180 °C. Relative complex permittivity and relative complex permeability were measured using a vector network analyzer (Agilent N5230A) at 2–18 GHz.

3 Results and discussion

Scheme 1 describes the fabrication procedure of the self-healing superhydrophobic F-PVDF/Fe_3O_4@PPy_x fibers. First, a PVDF/Fe_3O_4 fiber film was fabricated by electrospinning of a PVDF/Fe_3O_4 mixture. Second, PVDF/Fe_3O_4@PPy_x fiber film with a core–sheath structure was prepared through *in situ* chemical oxidative polymerization of pyrrole monomers, using $FeCl_3$ as an oxidant at room temperature. Lastly, a core–sheath structured F-PVDF/Fe_3O_4@PPy_x film was obtained by depositing FAS on the surface of the PVDF/Fe_3O_4@PPy_x film.

Figures 1(a) and 1(b) show SEM images of electrospun PVDF/Fe_3O_4 fiber films. From Fig. 1(a), the electrospun PVDF/Fe_3O_4 fiber film is composed of nonwoven, random fibers with an average diameter of 1.24 ± 0.14 μm. As shown in Fig. 1(b), the high-magnification SEM image of the electrospun PVDF/Fe_3O_4 fiber film clearly reveals that the surface of the PVDF/Fe_3O_4 fiber is very coarse, which may be caused by phase separation due to the interaction between hydrophobic PVDF and hydrophilic PVP-coated Fe_3O_4 nanoparticles during the electrospinning process. After *in situ* chemical oxidative polymerization of the pyrrole, PVDF/Fe_3O_4@$PPy_{0.075}$ fibers (PVDF/Fe_3O_4 fiber cores with PPy coating) were successfully fabricated. Meanwhile, the color of the flexible free-standing PVDF/Fe_3O_4@$PPy_{0.075}$ film (Fig. S2 in the ESM) changed from brown to black (insets of Figs. 1(a) and 1(c)). More nanoparticles with average diameters of 64 ±

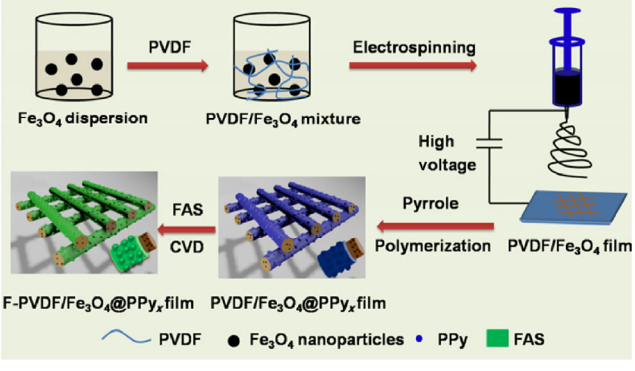

Scheme 1 Schematic illustration for fabrication of F-PVDF/Fe_3O_4@PPy_x fiber with core–sheath structure, which was obtained by electrospinning of a PVDF/Fe_3O_4 mixture and *in situ* chemical oxidative polymerization of pyrrole monomers, followed by CVD of FAS.

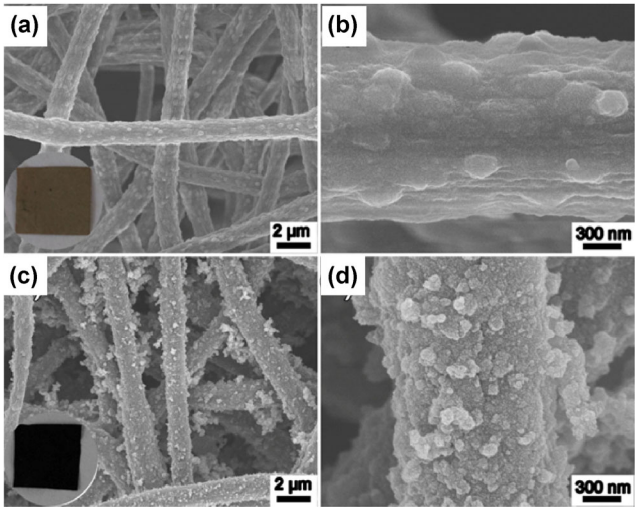

Figure 1 SEM images of (a), (b) PVDF/Fe_3O_4 fiber film and (c), (d) F-PVDF/Fe_3O_4@$PPy_{0.075}$ film; insets: digital photographs of PVDF/Fe_3O_4 fiber film and F-PVDF/Fe_3O_4@$PPy_{0.075}$ film.

12 nm were clearly observed on the surface of fibers of a typical F-PVDF/Fe_3O_4@$PPy_{0.075}$ film (Fig. 1(d)). Compared with PVDF/Fe_3O_4@$PPy_{0.075}$ film (Figs. S3(c) and S3(d) in the ESM), the surface of F-PVDF/Fe_3O_4@$PPy_{0.075}$ film (Figs. 1(c) and 1(d)) retains its micro/nanostructures after chemical modification by FAS. The molecular structure of PVDF/Fe_3O_4@$PPy_{0.075}$ film was studied by FT-IR spectroscopy (Fig. S4 in the ESM). The peak at 1,051 cm^{-1} is ascribed to =C–H in-plane vibrations [6], the peak at 1,561 cm^{-1} denotes the stretching vibration of C=C double bonds in PPy [20], and the weak band at 1,664 cm^{-1} is attributed to carbonyl groups indicating that PPy is slightly overoxidized during the polymerization process [20]. Based on this, these FT-IR results indicate that the above-mentioned nanoparticles are PPy.

Figure 2 displays scanning transmission electron microscopy (STEM) images of the F-PVDF/Fe_3O_4@$PPy_{0.075}$ film and the corresponding EDS element mapping images of Fe, Si and F. STEM bright-field imaging (Fig. 2(a)) further suggests that the F-PVDF/Fe_3O_4@$PPy_{0.075}$ fiber has a typical core–sheath structure. The EDS Fe mapping shown in Fig. 2(b) indicates that PVP-coated Fe_3O_4 nanoparticles are well-distributed in the F-PVDF/Fe_3O_4@$PPy_{0.075}$ fiber. The EDS elemental mappings of Si and F confirm a fairly uniform coating of FAS on the surface of the F-PVDF/Fe_3O_4@$PPy_{0.075}$ fiber, which contributes to the superhydrophobicity of the F-PVDF/Fe_3O_4@$PPy_{0.075}$ film.

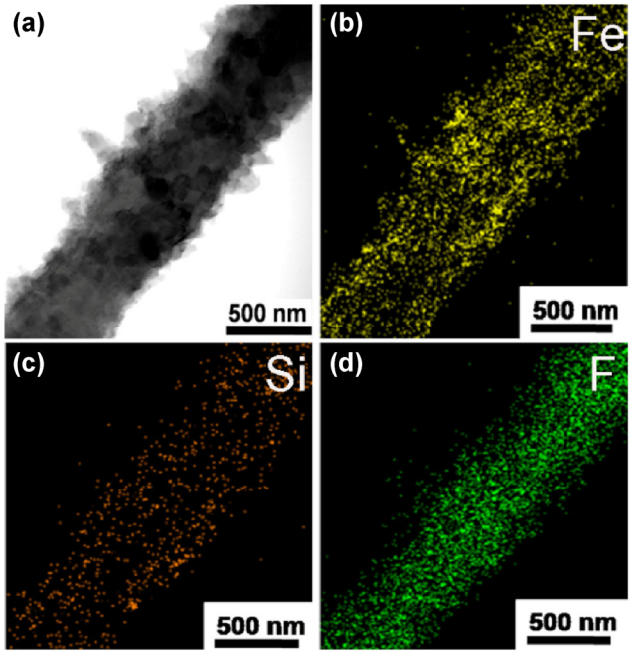

Figure 2 STEM bright-field image of (a) F-PVDF/Fe_3O_4@$PPy_{0.075}$ film and the corresponding elemental mapping analysis of (b) Fe, (c) Si and (d) F elements, respectively.

The electrical properties of the core–sheath structured F-PVDF/Fe_3O_4@PPy_x fiber films were also studied. As a sheath over the F-PVDF/Fe_3O_4@PPy_x fibers, PPy plays a vital role in their conductivity. The conductivity of F-PVDF/Fe_3O_4@PPy_x films with different pyrrole feedings from 0.05 to 0.10 g in the polymerization were measured by a standard four-probe method, which were calculated to be 4.4×10^{-3}, 3.6×10^{-2} and 6.2×10^{-1} S·cm^{-1} for F-PVDF/Fe_3O_4@$PPy_{0.05}$, F-PVDF/Fe_3O_4@$PPy_{0.075}$ and F-PVDF/Fe_3O_4@$PPy_{0.10}$ films, respectively. The results indicate that greater amounts of pyrrole during polymerization result in greater PPy contents in the core–sheath F-PVDF/Fe_3O_4@PPy_x fiber films (Table S1 in the ESM), improving their conductivity. The conductivity of the F-PVDF/Fe_3O_4@PPy_x films favors their use for EM absorption.

The magnetic properties of the obtained films were investigated using a vibrating sample magnetometer. The room-temperature magnetization curves shown in Fig. 3 suggest that the PVDF/Fe_3O_4, F-PVDF/Fe_3O_4@$PPy_{0.05}$, F-PVDF/Fe_3O_4@$PPy_{0.075}$ and F-PVDF/Fe_3O_4@$PPy_{0.10}$ films are superparamagnetic with saturation magnetizations (M_s) of 13.0, 12.0, 10.7, and 9.5 emu·g^{-1}, respectively. Compared with PVP-coated Fe_3O_4 nanoparticles (M_s = 56.5 emu·g^{-1}, Fig. S1 in the

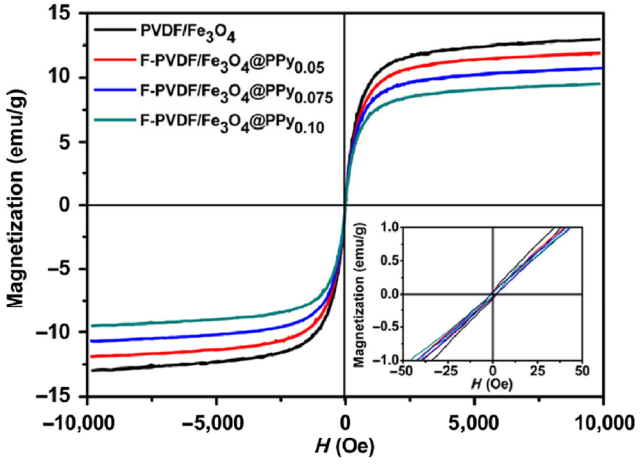

Figure 3 Magnetization curves of PVDF/Fe_3O_4 and F-PVDF/Fe_3O_4@PPy_x films measured at room temperature. The inset shows an enlarged view of magnetization of these samples.

ESM), the low M_s of these four samples could be attributed to their high polymer contents of 76.2 wt.%, 76.5 wt.%, 77.0 wt.% and 77.5 wt.%, respectively (Fig. S5 and Table S1 in the ESM). In addition, the remnant magnetization (M_r) of these samples is close to zero (inset of Fig. 3), which corresponds to superparamagnetic behavior. The magnetic properties of core–sheath structured F-PVDF/Fe_3O_4@PPy_x fiber films could be ascribed to superparamagnetic PVP-coated Fe_3O_4 nanoparticles shown in Fig. S1 (in the ESM).

Core–sheath structured F-PVDF/Fe_3O_4/@PPy_x fiber films, having dielectric PVDF combined with superparamagnetic Fe_3O_4 nanoparticles and uniform PPy conductive coating, are expected to have high-performance electromagnetic properties. In general, electromagnetic absorption properties of MAMs are closely associated with their electromagnetic parameters, relative complex permittivity ($\varepsilon_r = \varepsilon' - j\varepsilon''$) and relative complex permeability ($\mu_r = \mu' - j\mu''$). Real permittivity (ε') and real permeability (μ') represent the storage ability in regards to electric and magnetic energy, while the imaginary permittivity (ε'') and imaginary permeability (μ'') are related to the dissipation of electric and magnetic energy [9]. The electromagnetic parameters of PVDF/Fe_3O_4 and F-PVDF/Fe_3O_4@PPy_x films are shown in Figs. 4(a)–4(d) at 2–18 GHz. As depicted in Figs. 4(a) and 4(b), the values of ε' and ε'' for PVDF/Fe_3O_4 fiber film are 3.1 and 0.25, respectively, which are frequency independent. The values of ε' and ε'' for F-PVDF/Fe_3O_4@$PPy_{0.05}$, F-PVDF/Fe_3O_4@$PPy_{0.075}$ and F-PVDF/Fe_3O_4@$PPy_{0.10}$ films are higher than those of the PVDF/Fe_3O_4 fiber film, and increase with larger conductivity due to additional PPy coating.

As shown in Figs. 4(c) and 4(d), the μ' values for the PVDF/Fe_3O_4 fiber film and F-PVDF/Fe_3O_4@PPy_x films decline within the frequency range of 2–7 GHz and rise smoothly at 7–18 GHz, indicating normal resonance [12]. The values of μ'' for PVDF/Fe_3O_4 and F-PVDF/Fe_3O_4@PPy_x films are in the range of 0–0.1 except for μ'' of the F-PVDF/Fe_3O_4/$PPy_{0.10}$ film which is >0.1 in the frequency range of 11–18 GHz, indicating that the F-PVDF/Fe_3O_4/$PPy_{0.10}$ film has higher magnetic loss than the other three samples in the frequency range of 11–18 GHz, which might be caused by eddy current effects due to additional PPy coating.

In addition, the dielectric loss tangent ($\tan\delta_\varepsilon = \varepsilon''/\varepsilon'$) and the magnetic loss tangent ($\tan\delta_\mu = \mu''/\mu'$) were also calculated based on the permittivity and permeability of samples, as shown in Figs. 4(e) and 4(f). In the curves of tan δ_ε (Fig. 4e), tan δ_ε values for the core–sheath structured F-PVDF/Fe_3O_4@PPy_x fiber films are higher than 0.34 while this value for the PVDF/Fe_3O_4 fiber film is 0.05–0.09. According to electromagnetic theory, dielectric loss is usually affected by interfacial and electric dipole polarization [1, 21]. In particular, interfacial polarization arises when neighboring phases differ from each other in terms of dielectric constant, conductivity, or both [22]. In F-PVDF/Fe_3O_4@PPy_x fiber films, the interface is mainly formed between PVDF and PPy. The presence of PVDF may result in electric dipole polarization because of the electrophilic nature of the present fluorine [23]. In addition, the core–sheath structure of F-PVDF/Fe_3O_4@PPy_x fiber is another effect for increasing interfacial polarization. In Fig. 4(f), the variation tendency of tan δ_μ for PVDF/Fe_3O_4 and F-PVDF/Fe_3O_4@PPy_x films are almost identical to μ''. Magnetic loss generally arises from eddy current loss, which is natural in the GHz range [2, 24]. Eddy current loss can be calculated as

$$\mu'' \approx 2\pi\mu_0(\mu')^2\sigma d^2 f/3 \quad (1)$$

where σ and μ_0 are the electric conductivity and the permeability in vacuum, respectively. If the magnetic

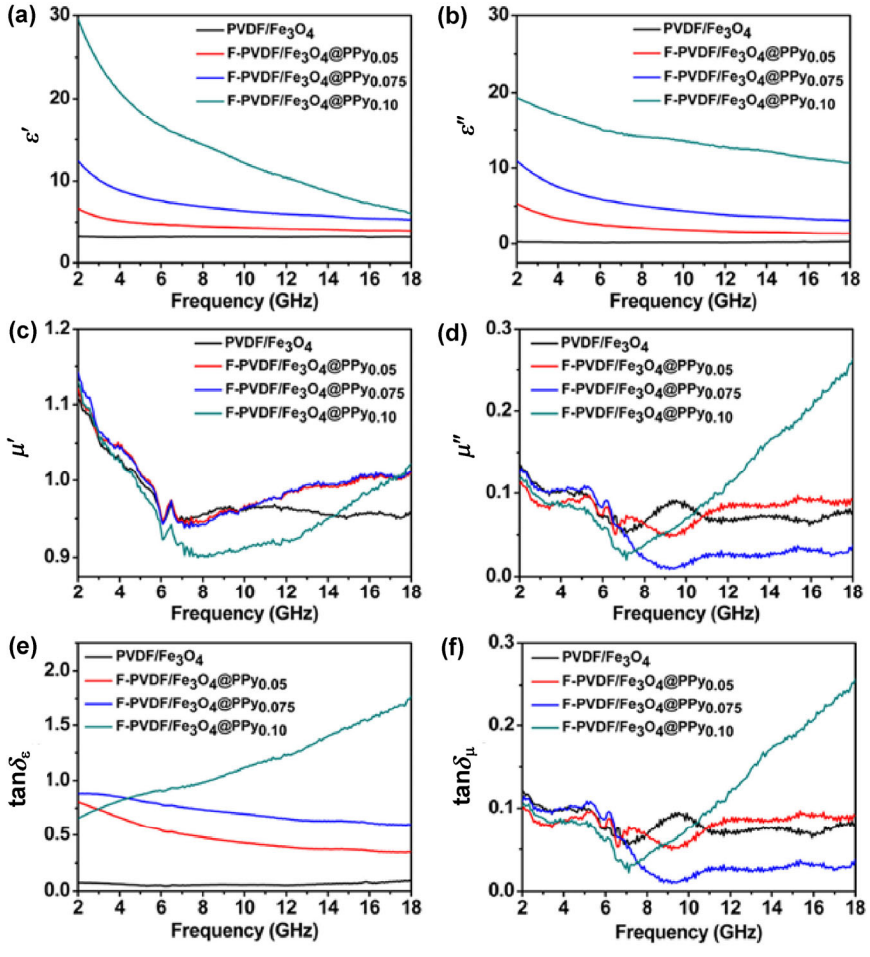

Figure 4 (a) Real parts and (b) imaginary parts of the relative complex permittivity; (c) real parts and (d) imaginary parts of the relative complex permeability; (e) dielectric tangent loss and (f) magnetic tangent loss of PVDF/Fe_3O_4 fiber film and core–sheath structured F-PVDF/Fe_3O_4@PPy_x fiber films in the frequency range of 2–18 GHz.

loss results from eddy current loss effects, the values of C_0 ($C_0 = \mu''(\mu')^{-2}f^{-1}$) should be constant when the frequency is changed [21]. C_0–f curves (Fig. S6 in the ESM) indicate that the values of C_0 for the four samples are almost constant within the frequency range of 11–18 GHz, indicating that the magnetic loss of these samples is caused by eddy current loss effects in this frequency range, and is ascribed to natural resonance at 2–11 GHz [25]. Conductivity is an important parameter that is related to eddy current loss. Despite the F-PVDF/Fe_3O_4@$PPy_{0.10}$ film having less magnetization than the others, the film has the highest conductivity among the four samples, which may result in the enhanced eddy current loss [26]. Therefore, the μ'' of F-PVDF/Fe_3O_4@$PPy_{0.10}$ film is higher than the other composites at 11–18 GHz. Compared with Fig. 4(e) and 4(f), the dielectric loss values of F-PVDF/Fe_3O_4@PPy_x films (0.34–1.75) are higher than the magnetic loss values (0–0.1), suggesting that their main loss mechanism is dielectric loss rather than magnetic loss [27, 28].

Due to the presence of PVDF, PPy and Fe_3O_4 nanoparticles, F-PVDF/Fe_3O_4@PPy_x or PVDF/Fe_3O_4 fiber films can possess both dielectric and magnetic properties, thus making films with special EM absorption properties. According to transmission line theory, R_L values can be calculated to evaluate the microwave absorption properties by

$$R_L(\text{dB}) = 20\log\left|\frac{Z_{in} - Z_0}{Z_{in} + Z_0}\right| \quad (2)$$

$$Z_{in} = Z_0\sqrt{\frac{\mu_r}{\varepsilon_r}}\tanh\left[j(2\pi fd/c)\sqrt{\varepsilon_r\mu_r} \right] \quad (3)$$

where Z_{in} is the input impedance of the absorber, Z_0 is the impedance of free space, μ_r and ε_r are respectively the relative complex permeability and permittivity, f is the frequency of microwaves, d is the thickness of the absorber, and c is the velocity of electromagnetic waves in free space [25]. The calculated R_L curves of PVDF/Fe_3O_4 and F-PVDF/Fe_3O_4@PPy_x films with different thickness at 2–18 GHz are shown in Fig. 5. For F-PVDF/Fe_3O_4@PPy_x films, the structure complexity and frequency impedance increase as sample thickness increases from 2.0 to 5.0 mm. The frequency impedance induces that the maximum R_L values gradually shift from high frequency regions to lower frequency regions, which is attributed to the shift of the matching range of dielectric and magnetic loss [6, 29]. As shown in Fig. 5(a), the maximum R_L of PVDF/Fe_3O_4 fiber film is lower than –5 dB, likely due to its low conductivity that limits the performance of dielectric loss, resulting in ineffective EM absorption [27]. For the F-PVDF/Fe_3O_4@$PPy_{0.05}$ film (Fig. 5(b)), the maximum R_L value reaches –48.8 dB at 7.7 GHz with a thickness of 5.0 mm, and the R_L below –10 dB is in the frequency between 6.0 and 9.7 GHz. For the F-PVDF/Fe_3O_4@$PPy_{0.075}$ film (Fig. 5(c)), the maximum R_L value is –21.5 dB at 16.8 GHz with a thickness of 2.0 mm, and the R_L below –10 dB is in the frequency range of 13.6–18.0 GHz. When the thickness is 2.5 mm, the maximum R_L value of F-PVDF/Fe_3O_4@$PPy_{0.075}$ is –17.7 dB at 12.8 GHz, and the R_L below –10 dB is in the frequency range of 10.6–16.5 GHz. Moreover, the frequency range where R_L is lower than –10 dB is 5.2–18.0 GHz with a corresponding thickness from 5.0 to 2.0 mm, revealing that the F-PVDF/Fe_3O_4@$PPy_{0.075}$ film has superior EM absorption performance from the X-band to the K_u-band. Meanwhile the maximum R_L value is no lower than –6 dB for the F-PVDF/Fe_3O_4@$PPy_{0.10}$ film (Fig. 5(d)), likely caused by two factors. First, the high conductivity of the F-PVDF/Fe_3O_4@$PPy_{0.10}$ film may result in skin effects and additional reflections at the surface between the F-PVDF/Fe_3O_4@$PPy_{0.10}$ film and air, which may decrease the EM absorption [27]. Second, the F-PVDF/Fe_3O_4@$PPy_{0.10}$ film has higher ε' and ε'' than those of PVDF/Fe_3O_4, F-PVDF/Fe_3O_4@$PPy_{0.05}$ and F-PVDF/Fe_3O_4@$PPy_{0.075}$ films, which does not favor impedance matching, leading to low dissipation of EM energy [30]. The EM absorption performance of PVDF/Fe_3O_4

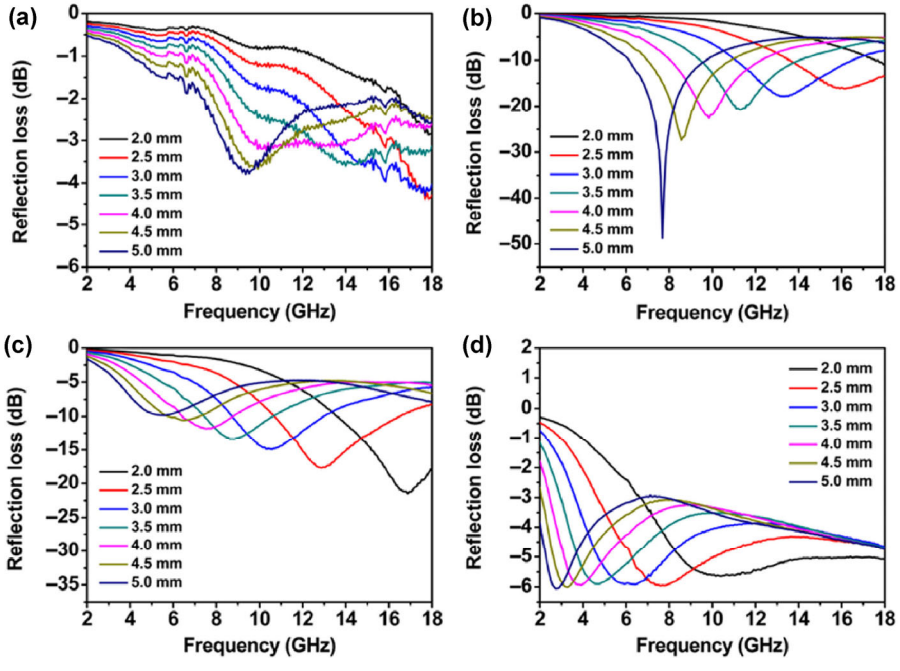

Figure 5 Reflection loss curves (a) PVDF/Fe_3O_4 fiber film, (b) F-PVDF/Fe_3O_4@$PPy_{0.05}$ film, (c) F-PVDF/Fe_3O_4@$PPy_{0.075}$ film, and (d) F-PVDF/Fe_3O_4@$PPy_{0.10}$ film with different thickness in the frequency range of 2–18 GHz.

and F-PVDF/Fe_3O_4@PPy_x films are illustrated in Table S2 (in the ESM).

The superhydrophobic nature of microwave absorbing films is also very important for their practical use in civil and military applications. The F-PVDF/Fe_3O_4@$PPy_{0.075}$ film displayed superior EM absorption, and was chosen to further investigate their self-healing and superhydrophobic properties. The as-prepared PVDF/Fe_3O_4@$PPy_{0.075}$ film was initially superhydrophilic with a water CA of 0° due to the presence of hydrophilic PPy. After being modified with low-surface-energy FAS, the film had a CA of 152.0° ± 0.5° (Fig. 6(a)) and a sliding angle of 6.5° (Fig. S7 in the ESM), indicating superhydrophobic and self-cleaning properties. Before and after FAS modification, the conductivities of PVDF/Fe_3O_4@$PPy_{0.075}$ and F-PVDF/Fe_3O_4@$PPy_{0.075}$ films were 4.0×10^{-2} S·cm^{-1} and 3.6×10^{-2} S·cm^{-1}, respectively, which indicates no obvious change in conductivity due to the low FAS content (only 0.5 wt.%). When the F-PVDF/Fe_3O_4@$PPy_{0.075}$ film was treated with air plasma etching (Fig. 6(a)), the etched F-PVDF/Fe_3O_4@$PPy_{0.075}$ film became superhydrophilic with a CA of 0°. The etched F-PVDF/Fe_3O_4@$PPy_{0.075}$ film spontaneously regained its superhydrophobicity when left in ambient conditions with a RH of 50% for 5 h. In addition, the etching–healing process could be repeated many times without obvious decreases in superhydrophobicity, as shown in Fig. 6(b). Mechanisms for the self-healing ability of F-PVDF/Fe_3O_4@$PPy_{0.075}$ film have been proposed previously [16, 17, 31]. When the film surface is damaged by air plasma etching, oxygen-containing polar groups are introduced into the fiber surface. FAS molecules on the fiber surface are further etched away and hydrophilic PPy is exposed, resulting in a superhydrophilic state. When the etched fiber film was put in a high humidity environment, the superhydrophilic film could absorb water impelling the migration of hydrophobic FAS underneath the damaged surface towards the surface to minimize the surface free energy, thus healing its superhydrophobicity. This allows for the superhydrophobic wettability of F-PVDF/Fe_3O_4@$PPy_{0.075}$ films to be restored.

EIS measurements were carried out to investigate and predict the anti-corrosive behavior of the films [32]. Figure 6(c) and 6(d) show Nyquist and Bode plots for

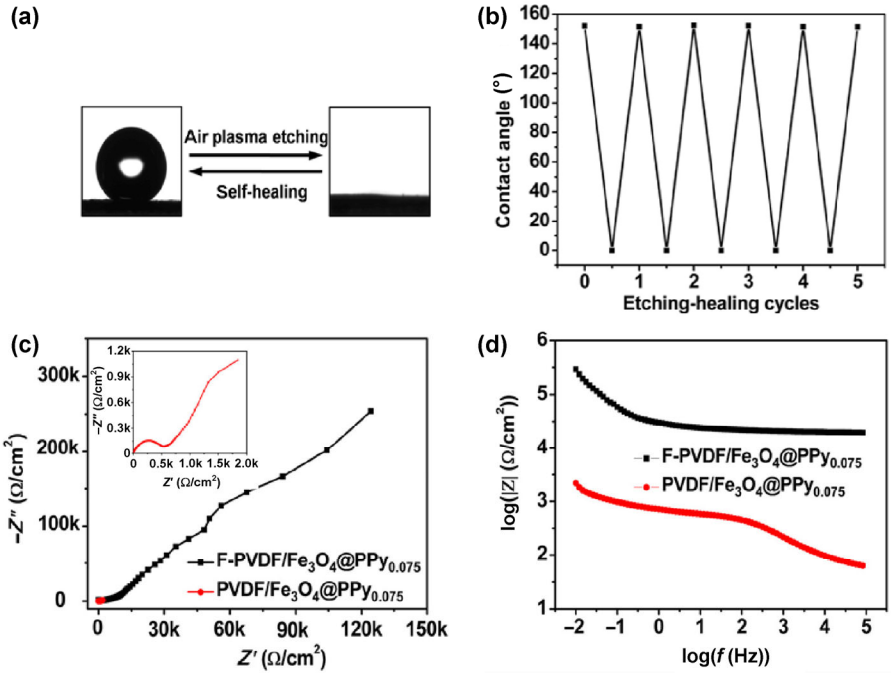

Figure 6 (a) Reversible transition between superhydrophobic (left) and superhydrophilic (right) states of the F-PVDF/Fe_3O_4@$PPy_{0.075}$ film upon air plasma etching and self-healing. (b) CA changes of the F-PVDF/Fe_3O_4@$PPy_{0.075}$ film upon air plasma etching and self-healing. (c) Nyquist plots and (d) Bode plots of F-PVDF/Fe_3O_4@$PPy_{0.075}$ film and PVDF/Fe_3O_4@$PPy_{0.075}$ film in 3.5 wt.% NaCl aqueous solution. The inset shows an enlarged view of the Nyquist plot for PVDF/Fe_3O_4@$PPy_{0.075}$ film.

F-PVDF/Fe_3O_4@$PPy_{0.075}$ and PVDF/Fe_3O_4@$PPy_{0.075}$ films in a 3.5 wt.% NaCl aqueous solution. As shown in Fig. 6(c), the F-PVDF/Fe_3O_4@$PPy_{0.075}$ film has an impedance value of approximately 1.2×10^5 $\Omega \cdot cm^{-2}$, which is 67 times higher than that of PVDF/Fe_3O_4@$PPy_{0.075}$ film, indicating that superhydrophobic F-PVDF/Fe_3O_4@$PPy_{0.075}$ film has good corrosion resistance [33]. Figure 6(d) shows the Bode plots (impedance modulus $|Z|$ as a function of frequency) of the two samples in a 3.5 wt.% NaCl aqueous solution. From Fig. 6(d), the F-PVDF/Fe_3O_4@$PPy_{0.075}$ film possesses a higher impedance modulus at low frequencies than PVDF/Fe_3O_4@$PPy_{0.075}$ film, further confirming that the superhydrophobic surface provides excellent corrosion protection.

4 Conclusions

In summary, we have successfully fabricated F-PVDF/Fe_3O_4@PPy_x core–sheath structured fiber films by electrospinning, *in situ* chemical oxidative polymerization and subsequent CVD of FAS. These F-PVDF/Fe_3O_4@$PPy_{0.075}$ fiber films exhibit self-healing and superhydrophobic abilities against damage by air plasma etching when left under ambient conditions with a RH of 50% for 5 h. The self-healing process can be repeated many times without any obvious decrease in superhydrophobicity. In addition, the maximum R_L value of the F-PVDF/Fe_3O_4@$PPy_{0.075}$ film reaches –21.5 dB at 16.8 GHz and the R_L below –10 dB is in the frequency range between 10.6 and 16.5 GHz with a thickness of 2.5 mm. Therefore, we believe that F-PVDF/Fe_3O_4@PPy_x fiber films with self-healing superhydrophobicity opens up a new avenue to extend the lifespan of MAMs for practical applications, especially in harsh environments.

Acknowledgements

The work is supported by the National Natural Science Foundation of China (Nos. 51273008, 51473008, and 21103006), Beijing Natural Science Foundation (No. 2132030) and the National Basic Research Program of China (No. 2012CB933200).

Electronic Supplementary Material: Supplementary material (characterizations of PVP-coated Fe_3O_4 nanoparticles, digital photographs of flexible free-standing core–sheath structured PVDF/Fe_3O_4@$PPy_{0.075}$ fiber film, SEM images of PVDF/Fe_3O_4@PPy_x films, FT-IR spectra of PVDF, PVDF/Fe_3O_4 fiber film and PVDF/Fe_3O_4@$PPy_{0.075}$ film, TGA curves, C_0–f curves of PVDF/Fe_3O_4 fiber film and F-PVDF/Fe_3O_4@PPy_x films, microwave absorption performance of PVDF/Fe_3O_4 fiber film and F-PVDF/Fe_3O_4@PPy_x films, photograph of sliding angle for F-PVDF/Fe_3O_4@$PPy_{0.075}$ film) is available in the online version of this article at http://dx.doi.org/10.1007/s12274-016-1094-x.

References

[1] Chen, D. Z.; Wang, G. S.; He, S.; Liu, J.; Guo, L.; Cao, M. S. Controllable fabrication of mono-dispersed RGO–hematite nanocomposites and their enhanced wave absorption properties. *J. Mater. Chem. A* **2013**, *1*, 5996–6003.

[2] Liu, X. F.; Chen, Y. X.; Cui, X. R.; Zeng, M.; Yu, R. H.; Wang, G. S. Flexible nanocomposites with enhanced microwave absorption properties based on Fe_3O_4/SiO_2 nanorods and polyvinylidene fluoride. *J. Mater. Chem. A* **2015**, *3*, 12197–12204.

[3] Liu, J. W.; Xu, J. J.; Che, R. C.; Chen, H. J.; Liu, M. M.; Liu, Z. W. Hierarchical Fe_3O_4@TiO_2 yolk–shell microspheres with enhanced microwave-absorption properties. *Chem. —Eur. J.* **2013**, *19*, 6746–6752.

[4] Wang, L.; Jia, X. L.; Li, Y. F.; Yang, F.; Zhang, L. Q.; Liu, L. P.; Ren, X.; Yang, H. T. Synthesis and microwave absorption property of flexible magnetic film based on graphene oxide/carbon nanotubes and Fe_3O_4 nanoparticles. *J. Mater. Chem. A* **2014**, *2*, 14940–14946.

[5] Lu, X. Y.; Wu, Y. Z.; Cai, H. Y.; Qu, X. Y.; Ni, L. M.; Teng, C.; Zhu, Y.; Jiang, L. Fe_3O_4 nanopearl decorated carbon nanotubes stemming from carbon onions with self-cleaning and microwave absorption properties. *RSC Adv.* **2015**, *5*, 54175–54181.

[6] Li, Y. B.; Chen, G.; Li, Q. H.; Qiu, G. Z.; Liu, X. H. Facile synthesis, magnetic and microwave absorption properties of Fe_3O_4/polypyrrole core/shell nanocomposite. *J. Alloy. Compd.* **2011**, *509*, 4104–4107.

[7] Oyharçabal, M.; Olinga, T.; Foulc, M.-P.; Lacomme, S.; Gontier, E.; Vigneras, V. Influence of the morphology of polyaniline on the microwave absorption properties of epoxy

polyaniline composites. *Compos. Sci. Technol.* **2013**, *74*, 107–112.

[8] Sun, Y. P.; Xiao, F.; Liu, X. G.; Feng, C.; Jin, C. G. Preparation and electromagnetic wave absorption properties of core–shell structured Fe_3O_4–polyaniline nanoparticles. *RSC Adv.* **2013**, *3*, 22554–22559.

[9] Zhou, W. C.; Hu, X. J.; Bai, X. X.; Zhou, S. Y.; Sun, C. H.; Yan, J.; Chen, P. Synthesis and electromagnetic, microwave absorbing properties of core-shell Fe_3O_4-poly(3,4-ethylenedioxythiophene) microspheres. *ACS Appl. Mater. Interfaces* **2011**, *3*, 3839–3845.

[10] Xiang, J.; Li, J. L.; Zhang, X. H.; Ye, Q.; Xu, J. H.; Shen, X. Q. Magnetic carbon nanofibers containing uniformly dispersed Fe/Co/Ni nanoparticles as stable and high-performance electromagnetic wave absorbers. *J. Mater. Chem. A* **2014**, *2*, 16905–16914.

[11] Chen, Y.-H.; Huang, Z.-H.; Lu, M.-M.; Cao, W.-Q.; Yuan, J.; Zhang, D.-Q.; Cao, M.-S. 3D Fe_3O_4 nanocrystals decorating carbon nanotubes to tune electromagnetic properties and enhance microwave absorption capacity. *J. Mater. Chem. A* **2015**, *3*, 12621–12625.

[12] Cui, C. K.; Du, Y. C.; Li, T. H.; Zheng, X. Y.; Wang, X. H.; Han, X. J.; Xu, P. Synthesis of electromagnetic functionalized Fe_3O_4 microspheres/polyaniline composites by two-step oxidative polymerization. *J. Phys. Chem. B* **2012**, *116*, 9523–9531.

[13] Liu, T.; Pang, Y.; Zhu, M.; Kobayashi, S. Microporous Co@CoO nanoparticles with superior microwave absorption properties. *Nanoscale* **2014**, *6*, 2447–2454.

[14] Jiang, L.; Zhao, Y.; Zhai, J. A lotus-leaf-like superhydrophobic surface: A porous microsphere/nanofiber composite film prepared by electrohydrodynamics. *Angew. Chem.* **2004**, *116*, 4438–4441.

[15] Manna, U.; Lynn, D. M. Restoration of superhydrophobicity in crushed polymer films by treatment with water: Self-healing and recovery of damaged topographic features aided by an unlikely source. *Adv. Mater.* **2013**, *25*, 5104–5108.

[16] Li, Y.; Li, L.; Sun, J. Q. Bioinspired self-healing superhydrophobic coatings. *Angew. Chem., Int. Ed.* **2010**, *49*, 6129–6133.

[17] Zhou, H.; Wang, H. X.; Niu, H. T.; Gestos, A.; Lin, T. Robust, self-healing superamphiphobic fabrics prepared by two-step coating of fluoro-containing polymer, fluoroalkyl silane, and modified silica nanoparticles. *Adv. Func. Mater.* **2013**, *23*, 1664–1670.

[18] Lu, X. Y.; Niu, M.; Qiao, R. R.; Gao, M. Y. Superdispersible PVP-coated Fe_3O_4 nanocrystals prepared by a "one-pot" reaction. *J. Phys. Chem. B* **2008**, *112*, 14390–14393.

[19] Maity, D.; Kale, S. N.; Kaul-Ghanekar, R.; Xue, J. M.; Ding, J. Studies of magnetite nanoparticles synthesized by thermal decomposition of iron (III) acetylacetonate in tri(ethylene glycol). *J. Magn. Magn. Mater.* **2009**, *321*, 3093–3098.

[20] Lu, G. W.; Li, C.; Shi, G. Q. Polypyrrole micro- and nanowires synthesized by electrochemical polymerization of pyrrole in the aqueous solutions of pyrenesulfonic acid. *Polymer* **2006**, *47*, 1778–1784.

[21] Zhang, X. J.; Wang, G. S.; Cao, W. Q.; Wei, Y. Z.; Liang, J. F.; Guo, L.; Cao, M. S. Enhanced microwave absorption property of reduced graphene oxide (RGO)-$MnFe_2O_4$ nanocomposites and polyvinylidene fluoride. *ACS Appl. Mater. Interfaces* **2014**, *6*, 7471–7478.

[22] Liu, T.; Zhou, P. H.; Xie, J. L.; Deng, L. J. The hierarchical architecture effect on the microwave absorption properties of cobalt composites. *J. Appl. Phys.* **2011**, *110*, 033918.

[23] Meng, X. M.; Zhang, X. J.; Lu, C.; Pan, Y. F.; Wang, G. S. Enhanced absorbing properties of three-phase composites based on a thermoplastic-ceramic matrix ($BaTiO_3$ + PVDF) and carbon black nanoparticles. *J. Mater. Chem. A* **2014**, *2*, 18725–18730.

[24] Du, Y. C.; Liu, W. W.; Qiang, R.; Wang, Y.; Han, X. J.; Ma, J.; Xu, P. Shell thickness-dependent microwave absorption of core–shell Fe_3O_4@C composites. *ACS Appl. Mater. Interfaces* **2014**, *6*, 12997–13006.

[25] Wang, G. Z.; Gao, Z.; Wan, G. P.; Lin, S. W.; Yang, P.; Qin, Y. High densities of magnetic nanoparticles supported on graphene fabricated by atomic layer deposition and their use as efficient synergistic microwave absorbers. *Nano Res.* **2014**, *7*, 704–716.

[26] Liu, X. F.; Cui, X. R.; Chen, Y. X.; Zhang, X.-J.; Yu, R. H.; Wang, G.-S.; Ma, H. Modulation of electromagnetic wave absorption by carbon shell thickness in carbon encapsulated magnetite nanospindles–poly(vinylidene fluoride) composites. *Carbon* **2015**, *95*, 870–878.

[27] Cao, M. S.; Yang, J.; Song, W. L.; Zhang, D. Q.; Wen, B.; Jin, H. B.; Hou, Z. L.; Yuan, J. Ferroferric oxide/multiwalled carbon nanotube vs. polyaniline/ferroferric oxide/multiwalled carbon nanotube multiheterostructures for highly effective microwave absorption. *ACS Appl. Mater. Interfaces* **2012**, *4*, 6949–6956.

[28] Wang, L.; Huang, Y.; Sun, X.; Huang, H. J.; Liu, P. B.; Zong, M.; Wang, Y. Synthesis and microwave absorption enhancement of graphene@Fe_3O_4@SiO_2@NiO nanosheet hierarchical structures. *Nanoscale* **2014**, *6*, 3157–3164.

[29] Wang, H.; Dai, Y. Y.; Geng, D. Y.; Ma, S.; Li, D.; An, J.; He, J.; Liu, W.; Zhang, Z. D. Co_xNi_{100-x} nanoparticles

encapsulated by curved graphite layers: Controlled *in situ* metal-catalytic preparation and broadband microwave absorption. *Nanoscale* **2015**, *7*, 17312–17319.

[30] Zhou, W. C.; Hu, X. J.; Sun, C. H.; Yan, J.; Zhou, S. Y.; Chen, P. Microwave absorbing properties of Fe_3O_4-poly(3,4-ethylenedioxythiophene) hybrids in low-frequency band. *Polym. Advan. Technol.* **2014**, *25*, 83–88.

[31] Chen, S. S.; Li, X.; Li, Y.; Sun, J. Q. Intumescent flame-retardant and self-healing superhydrophobic coatings on cotton fabric. *ACS Nano* **2015**, *9*, 4070–4076.

[32] Su, F. H.; Yao, K. Facile fabrication of superhydrophobic surface with excellent mechanical abrasion and corrosion resistance on copper substrate by a novel method. *ACS Appl. Mater. Interfaces* **2014**, *6*, 8762–8770.

[33] Xu, W. J.; Song, J. L.; Sun, J.; Lu, Y.; Yu, Z. Y. Rapid fabrication of large-area, corrosion-resistant superhydrophobic Mg alloy surfaces. *ACS Appl. Mater. Interfaces* **2011**, *3*, 4404–4414.